PHYSICAL REVIEW B **75**, 041404(R) (2007)

Coulomb screening and collective excitations in a graphene bilayer

Xue-Feng Wang and Tapash Chakraborty
Department of Physics and Astronomy, The University of Manitoba, Winnipeg, Canada R3T 2N2
(Received 27 November 2006; published 16 January 2007)

We have investigated the Coulomb screening properties and collective excitations in a graphene bilayer. The static screening effect is anisotropic and is much stronger in the undoped graphene bilayer than in a monolayer graphene. The dynamic screening shows the properties of a Dirac gas at low frequency and that of a Fermi gas at high frequency. The transition from the Dirac to the Fermi gas is also observed in the plasmon spectrum. Finally, we find that an electron gas in a doped graphene bilayer has quite similar properties as those of a Fermi gas in materials containing two energy valleys.

DOI: 10.1103/PhysRevB.75.041404 PACS number(s): 71.10.−w, 75.10.Lp, 75.70.Ak, 71.70.Gm

The realization of monolayer and the bilayer graphene—the two-dimensional crystal of one and two layers of carbon atoms—has opened a door for the exploration of the fundamental physics and also fabrication of nanoelectronic devices.[1–3] Being different from multilayer graphene or graphite, monolayer and bilayer graphene are intrinsically zero-gap semiconductors. Monolayer graphene has the properties of a chiral Dirac gas while the graphene bilayer has the energy band of a chiral Fermi gas at high energies with several Dirac points at the bottom of the band.[4–7] Consequently, a comparison of the physical properties between them would offer new understanding and provide interesting predictions about the different behaviors between the charged chiral-Dirac and Fermi gases.

In normal two-dimensional semiconductors, the many-body effects on the Coulomb interaction have been extensively studied using different methods. One of the most successful and widely accepted approaches is the random-phase approximation (RPA). In this approximation it is assumed that only the single-particle excitations of the same wave vector as the Coulomb interaction plays an effective role in the screening process while the effects of others having different wave vectors cancel out. Use of the RPA is justified when the electron-electron interaction is strong enough that quantum coherence does not dominate. In the past years, there have been a few studies reported in the literature on Coulomb screening and the collective excitation spectrum in the monolayer graphene using the RPA.[8–12] In this paper, we employ the RPA to address some of the interesting properties of Coulomb screening and collective excitations in a graphene bilayer.

A graphene bilayer is formed by stacking two graphene layers in the same way as the stacking occurs in graphite—i.e., the Bernal stacking.[4–7] Each graphene layer has a hexagonal (honeycomb) carbon lattice [Fig. 1(a)] which is composed of two periodic sublattices A and B [Fig. 1(b)]. In other words, there are two inequivalent lattice sites with atoms A and B in each unit cell of the periodic lattice. The two sublattices are displaced from each other along an edge of the hexagons by a distance of a_0=1.42 Å. In a graphene bilayer, there are four inequivalent sites in each unit cell, with atoms A and B at the top and A' and B' at the bottom. In the case of Bernal stacking, the two graphene layers are arranged in such a way that the A sublattice is exactly on top of the sublattice B' with a vertical separation of b_0=3.4 Å,[13] as shown in Figs. 1(a) and 1(b). The system can be described by a tight-binding model[5] characterized by three coupling parameters: γ_0=3.16 eV between the atoms A and B or A' and B' (intralayer coupling), γ_1=0.39 eV between A and B' (the direct interlayer coupling), and γ_3=0.315 eV between A' and B, A and A', or B and B' (the indirect interlayer coupling).

In the k space, the graphene bilayer has the same hexagonal Brillouin zone as that of a graphene monolayer. Its physical properties are mainly determined by the energy spectrum and the wave function near the two inequivalent corners of the Brillouin zone, K and K', where the π^* conduction band and the π valence band meet at the Fermi surface.[14] Due to the strong interlayer coupling (the π-orbit overlap) both the conduction band and the valence band in a bilayer are split

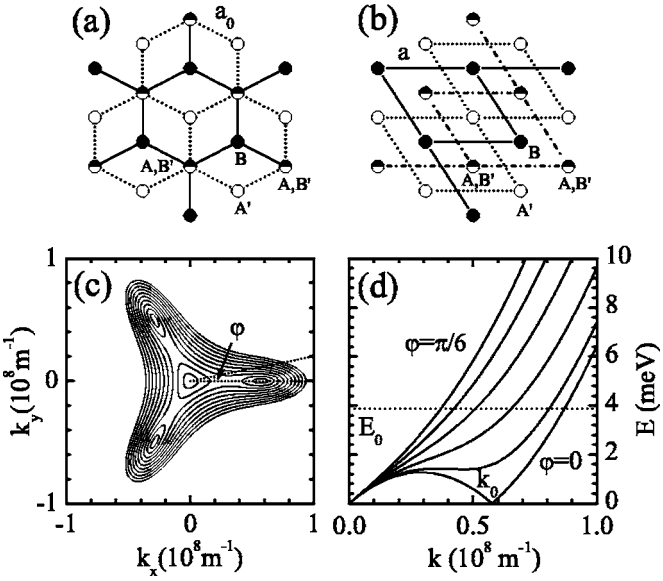

FIG. 1. (a) The hexagonal lattice of the top graphene layer (solid line) and the bottom layer (dotted line). (b) Periodic sublattices A and B' (dash-dotted lines), B (solid lines), and A' (dotted). In (a) and (b), the atoms of the sublattice A (B'), B, and A' are denoted by semisolid, solid, and open circles, respectively. (c) The contour lines of the energy in the k_x-k_y plane near the K point. The corresponding energies, starting with the innermost curve, are $0.1E_0$ to E_0 with an increment of $0.1E_0$. (d) The energy spectrum for equally separated φ from 0 to $\pi/6$ (curves with increasing energy).

by an energy of ~0.4 eV near the K and K' valleys.[7,13,15] Since this energy splitting is larger than the energy range we are interested in from the bottom of the energy band, we take into account only the upper valence band and the lower conduction band. The graphene bilayer cannot be treated as two independent graphene monolayers with the interlayer coupling as a perturbation because of the strong interlayer overlap of the π orbits. In contrast, the perturbation treatment of the interlayer coupling is valid for a normal double-quantum-well system[16] or in an intercalated graphite.[17]

In the effective-mass approximation,[4,5] the electrons in the K valley are described by a Hamiltonian with a mixture of the linear and the quadratic terms of k:

$$H_K = \frac{\hbar^2}{2m^*}\begin{pmatrix} 0 & k_-^2 \\ k_+^2 & 0 \end{pmatrix} - \frac{\hbar^2 k_0}{2m^*}\begin{pmatrix} 0 & k_+ \\ k_- & 0 \end{pmatrix}, \tag{1}$$

with $k_\pm = k_x \pm ik_y$ and $\boldsymbol{k}=(k_x,k_y)$ being measured from the K point. The effective mass of the quadratic term is $m^* = 2\hbar^2\gamma_1/(3a_0\gamma_0)^2 \approx 0.033m_0$ with m_0 the free electron mass and the "light" velocity of the linear term is $v_0 = \hbar k_0/2m^* = 3a_0\gamma_3/2\hbar \approx 10^5$ m/s with $k_0 \approx 10^8/\sqrt{3}$ m^{-1}.

The eigenfunction of the above Hamiltonian is $\Psi_{\boldsymbol{k}}^{\lambda}(\boldsymbol{r}) = \frac{e^{i\boldsymbol{k}\cdot\boldsymbol{r}}}{\sqrt{2}}\begin{pmatrix} e^{i\phi_{\boldsymbol{k}}} \\ \lambda \end{pmatrix}$ with the energy $E_{\boldsymbol{k}}^{\lambda} = \lambda\hbar^2 k\sqrt{k^2 - 2k_0 k\cos 3\varphi + k_0^2}/2m^*$ and the pseudospin angle $\lambda\phi_{\boldsymbol{k}}$. Here $\varphi = \arg(k_+)$, $\phi = \arg(ke^{-2i\varphi} - k_0 e^{i\varphi})$ with $\arg(z)$ being the argument θ of a complex $z = |z|e^{i\theta}$ and $\lambda = 1(-1)$ for the conduction (valence) band.

For $k \gg k_0$ the electron states are chiral with $\phi = -2\varphi$ and have an approximately isotropic parabolic energy dispersion $E_{\boldsymbol{k}}^{\lambda} = \lambda\hbar^2 k^2/2m^*$. Near $k = k_0$, the energy dispersion becomes highly anisotropic as shown in Figs. 1(c) and 1(d). The corresponding characteristic energy is $E_0 = \hbar^2 k_0^2/2m^* = 3.9$ meV. At $E=0$, where the Fermi energy is located in the undoped graphene bilayer, there are four contact points between the conduction and valence bands: one at $k=0$, the center of the valley, and the three satellites at $k=k_0$ in the directions of $\varphi = 0$, $2\pi/3$, and $4\pi/3$. They can be treated as four Dirac points because the electronic states near each point have a linear energy dispersion and have the same chirality as those near a Dirac point in the monolayer graphene. However, compared to the graphene monolayer, the energy dispersion here is anisotropic and the "light" velocity is about 10 times slower. As illustrated in Figs. 1(c) and 1(d), there is an energy pocket with a depth of about $E_0/4$ at each Dirac point. The above peculiar characteristics of the graphene bilayer makes it quite different from the graphene monolayer in their Coulomb screening properties as described in the following.

Just as for the case of the graphene monolayer[10] and other spin systems,[16] we find that the dielectric matrix of a graphene bilayer is again a unit matrix multiplied by a dielectric function

$$\hat{\varepsilon}(q,\omega) = 1 - v_q \hat{\Pi}_0(\mathbf{q},\omega), \tag{2}$$

with the bare Coulomb interaction $v_q = e^2/(2\varepsilon_0 q)$ and the electron-hole propagator

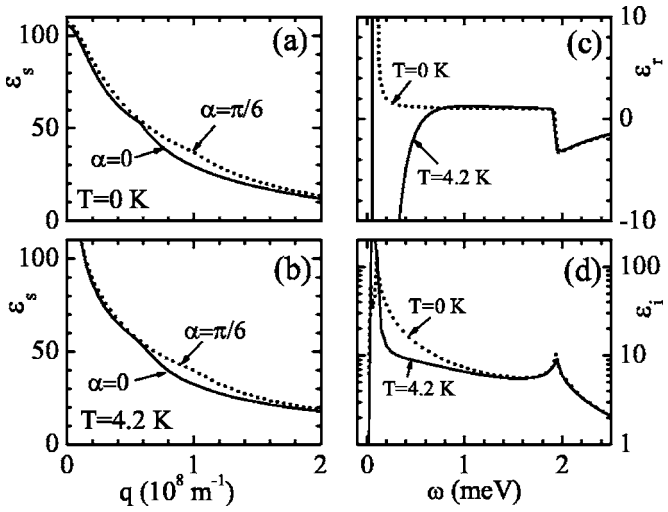

FIG. 2. (a) The static dielectric function ε_s vs the wave vector q along the direction $\alpha=0$ (solid line) and $\pi/6$ (dotted line) at $T=0$. (b) The same as (a) but at $T=4.2$ K. (c) The real part of the dielectric function ε_r vs frequency ω at $T=0$ (dotted line) and at $T=4.2$ K (solid line). (d) The imaginary part of the dielectric function ε_i vs ω at $T=0$ (dotted line) and at $T=4.2$ K (solid line). In (c) and (d), $q = 0.005\times 10^8$ m^{-1} and $\alpha=0$. In the limit $\omega\to\infty$, ε_r gradually approaches to one while ε_i approaches zero.

$$\hat{\Pi}(\mathbf{q},\omega) = 4\sum_{\lambda,\lambda',k} |g_{\boldsymbol{k}}^{\lambda,\lambda'}(\boldsymbol{q})|^2 \frac{f(E_{k+q}^{\lambda'}) - f(E_k^{\lambda})}{\omega + E_{k+q}^{\lambda'} - E_k^{\lambda} + i\delta}. \tag{3}$$

The factor of 4 comes from the degenerate two spins and two valleys at K and K', $f(x)$ is the Fermi function, and the vertex factor reads $|g_{\boldsymbol{k}}^{\lambda,\lambda'}(\boldsymbol{q})|^2 = [1+\lambda\lambda'\cos(\phi_{\boldsymbol{k}} - \phi_{\boldsymbol{k}+\boldsymbol{q}})]/2$. Near the central Dirac point at $k=0$, intraband backward scattering and interband vertical Coulomb scattering are forbidden and $|g_{\boldsymbol{k}}^{\lambda,-\lambda}(0)|^2 = |g_{\boldsymbol{k}}^{\lambda,\lambda}(-2\boldsymbol{k})|^2 = 0$. The same rules also hold for the three satellite Dirac points. For a large k ($k \gg k_0$), $|g_{\boldsymbol{k}}^{\lambda,-\lambda}(0)|^2 = |g_{\boldsymbol{k}}^{\lambda,-\lambda}(-2\boldsymbol{k})|^2 = 0$ but $|g_{\boldsymbol{k}}^{\lambda,\lambda}(-2\boldsymbol{k})|^2 = 1$; i.e., the intraband backward transition is allowed but both the interband backward and vertical transitions are forbidden. The above selection rules together with the energy dispersion of the carriers in the graphene bilayer indicate that the electrons (holes) close to the bottom (top) of the conduction (valence) band have very different behaviors from those away from the bottom (top).

Note that in a graphene monolayer the dielectric function $\hat{\varepsilon}$ is invariant if all the parameters with energy units ω, E_F, and k_BT and with wave vector units $\boldsymbol{k}$ and $\boldsymbol{q}$ vary proportionally because of the linear energy dispersion of the Dirac gas.[10] As a result, the dielectric function and the plasmon dispersion is uniform for systems with proportional parameters. In a graphene bilayer, however, this is not true anymore because of the nonlinear energy dispersion.

Coulomb screening. The static dielectric function at zero temperature versus q is plotted in Fig. 2(a). Its long-wavelength limit is given by the properties of the four Dirac points. The central point has an isotropic "light" velocity $v_0 = \hbar k_0/(2m^*) = 10^5$ m/s while the satellite ones have the elliptic form of equienergy lines with a minimum "light" ve-

locity equal to v_0 along their radical direction and a maximum of $3v_0$ along the azimuthal direction. The static dielectric constant at $q=0$ is estimated to be $\varepsilon_s=1+3e^2/(8\varepsilon_0\hbar v_0)\approx 105$. This value is much larger than that of the graphene monolayer (4.5).[10] This means that the long-range Coulomb interaction is much more strongly screened for the bilayer system, thanks to a much larger density of states near the Fermi energy in a graphene bilayer.

Another characteristic of the graphene bilayer is its screening anisotropy, especially for scattering at a distance range of about 10 nm. This is shown by the difference between the solid and dotted curves in Fig. 2, corresponding to the directions of $\boldsymbol{q}$ pointing to any satellite from the central Dirac points ($\alpha=0$) or connecting any two satellites ($\alpha=\pi/6$), respectively. Here α is the angle between $\boldsymbol{q}$ and the x axis. At $q=\sqrt{3}k_0=10^8$ m^{-1}, the wave vector distance between any two satellite Dirac points, the anisotropy of ε_s reaches its maximum with a mismatch of 20% along the different directions. The shoulder near $q=k_0=0.58\times 10^8$ m^{-1} in the solid curve reflects the strong scattering between the carriers in the central and the $\varphi=0$ setellite Dirac points. At a finite temperature, the energy pockets near the Dirac points are partially occupied and the intraband scattering strength is greatly enhanced. As a result, the static dielectric function near $q=0$ increases rapidly, as shown in Fig. 2(b) at $T=4.2$ K.

In order to have a complete picture of the Coulomb screening and an insight for understanding the plasmon spectrum in graphene bilayers we have calculated the real and imaginary parts of the dynamic dielectric function versus the energy for a small wave vector $q=0.005$ along $\alpha=0$ at $T=0$ and at $T=4.2$ K in Figs. 2(c) and 2(d).

For $\omega>E_0/2$, the dielectric function of a graphene bilayer is similar to that of a normal Fermi gas and its temperature dependence is weak. The step of ε_r and the peak of ε_i near $\omega=E_0/2=2$ meV correspond to the single-particle excitation coupling states with a vanishing group velocity and having wave vectors located near the middle between the central and the satellite Dirac points. For small ω, however, the dielectric function becomes more sensitive to the temperature and shows characteristics of the Dirac gas. One sign of the Dirac gas is the lack of Coulomb screening ($\varepsilon_r\approx 1$) in the energy window between 1 and 2 meV. Another sign is that a low-energy plasmon mode appears only at a finite temperature. As shown in Fig. 2(c), the ε_r has no negative value for the energy $\omega<E_0/2$ at $T=0$ but evolves into a deep negative dip at a finite temperature $T=4.2$ K, when the energy pockets near the Dirac points are partially occupied. As a result, one observes a weakly Landau damped plasmon mode of dispersion $\omega\sim\sqrt{q}$ at $T=0$ and a couple at finite temperatures.

Collective excitation. In Fig. 3(a), we calculate the plasmon spectrum of an intrinsic graphene bilayer ($E_F=0$). The dispersion of the weakly Landau damped mode is indicated by the thick curve and has a $\sqrt{q}$ dependence. Interestingly, the plasmon mode exists only at the energy higher than $E_0/2$—i.e., double the depth of the energy pockets in the Dirac points. At a finite temperature $T=4.2$ K, another weakly damped plasmon mode shows up at the energy lower than $E_0/2$ and also has a dispersion of $\sqrt{q}$ near $q=0$, as

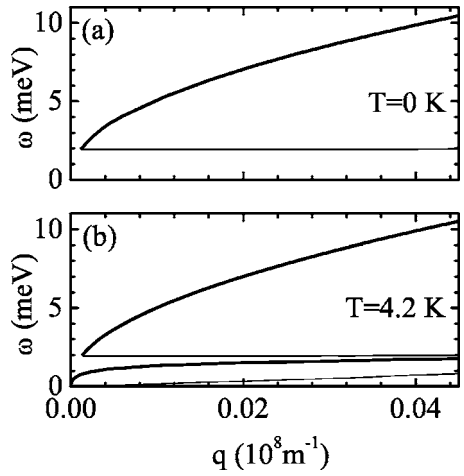

FIG. 3. The plasmon spectrum of an undoped graphene bilayer at $T=0$ (a) and at $T=4.2$ K (b). The thick curves indicate the weakly Landau damped modes while the thin curves represent the strongly damped modes.

illustrated in Fig. 3(b). The plasmon mode of higher energy that exists at $T=0$ is not sensitive to the temperature. This temperature dependence of the low- and high-energy plasmon spectra represents the marked difference between the electron gases having linear (without the collective excitation) and quadratic (with the collective excitation) energy dispersion at $T=0$. We have established earlier that the collective excitations appear only at a finite temperature for the Dirac gas.[10] The electronic states in a graphene bilayer are similar to the Fermi type at high energies but revert to a Dirac type at low energies.

The carrier density of the system can be changed by doping.[7] For a typical doping density of 10^{12} cm^{-2},[5,7] the Fermi energy is high enough from the conduction bottom and the linear k term in the Hamiltonian can be neglected. The electrons then have a quadratic dispersion but with chirality and $\phi=-2\varphi$. Near $q=0$, the plasmon dispersion in a doped graphene bilayer has again a $\sqrt{q}$ dispersion as shown by the solid curve in Fig. 4 and shares the same dispersion $\omega_p^{2D}=[n_e e^2 q/2\varepsilon_0 m^*]^{1/2}$ with a normal two-dimensional Fermi

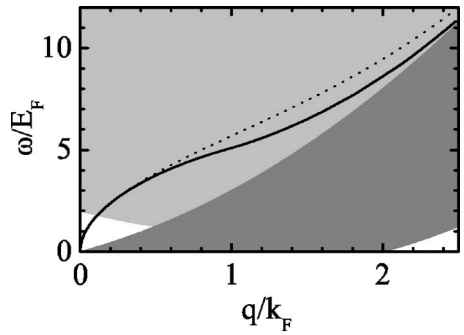

FIG. 4. The plasmon spectrum of a doped graphene bilayer (solid curve) with a typical carrier density of 10^{12} cm^{-2}. Correspondingly, $E_F=36.3$ meV and $k_F=1.77\times 10^8$ m^{-1}. The plasmon spectrum in the same system but without chirality is plotted as a dotted curve for comparison. Intraband (dark shaded) and interband (light shaded) single-particle continua are also shown.

gas. To see the effect of the chirality, we plot as a dotted curve the plasmon dispersion of a normal two-dimensional Fermi gas with two valleys, for comparison. The two curves overlap for the small q but separate as q increases. The maximum difference in the dispersion appears near $q=\sqrt{2}k_F$ when $\boldsymbol{k}$ and $\boldsymbol{k}+\boldsymbol{q}$ form a right angle in the Fermi plane and the corresponding transition is forbidden in the graphene bilayer due to its chirality.

In summary, we have explored the Coulomb screening properties and the collective excitation modes in a graphene bilayer. In an undoped system, the static dielectric constant is much larger than that in a graphene monolayer due to the existence of four Dirac points in each energy valley and the much lower "light" velocity of the Dirac points than the one in a graphene monolayer. The Coulomb screening also shows a strong anisotropy, especially near the wave vector $q=\sqrt{3}k_0$. The dynamic Coulomb screening has the characteristics of a Dirac gas on the low-energy side and those of a Fermi gas on the high-energy side. This transition from the Dirac to a Fermi gas is also reflected in the plasmon dispersion as the wave vector or the energy increases from zero. In a doped bilayer system, the long-wave-vector limit of the collective excitation has the same property as in a normal two-dimensional Fermi gas with two valleys.

The work has been supported by the Canada Research Chair Program and a Canadian Foundation for Innovation (CFI) grant.

[1] T. Ando, in *Nano-physics & Bio-electronics: A new Odyssey*, edited by T. Chakraborty, F. Peeters, and U. Sivan (Elsevier, Amsterdam, 2002), Chap. 1.

[2] A. K. Geim and K. S. Novoselov (unpublished).

[3] A. H. Castro Neto, F. Guinea, and N. M. Peres, Phys. World **19**, 33 (2006).

[4] E. McCann and V. I. Fal'ko, Phys. Rev. Lett. **96**, 086805 (2006); K. S. Novoselov *et al.*, Nat. Phys. **2**, 177 (2006); M. I. Katsnelson, K. S. Novoselov, and A. K. Geim *ibid.*, **2**, 620 (2006).

[5] M. Koshino and T. Ando, Phys. Rev. B **73**, 245403 (2006).

[6] J. Nilsson, A. H. Castro Neto, N. M. R. Peres, and F. Guinea, Phys. Rev. B **73**, 214418 (2006).

[7] T. Ohta, A. Bostwick, T. Seyller, K. Horn, and E. Rotenberg, Science **313**, 951 (2006).

[8] T. Ando, J. Phys. Soc. Jpn. **75**, 074716 (2006).

[9] D. V. Khveshchenko, Phys. Rev. B **74**, 161402(R) (2006).

[10] X. F. Wang and T. Chakraborty, Phys. Rev. B **75**, 033408 (2007).

[11] O. Vafek, Phys. Rev. Lett. **97**, 266406 (2006).

[12] E. H. Hwang and S. Das Sarma, cond-mat/0610561 (unpublished).

[13] S. B. Trickey, F. Müller-Plathe, G. H. F. Diercksen, and J. C. Boettger, Phys. Rev. B **45**, 4460 (1992).

[14] P. R. Wallace, Phys. Rev. **71**, 622 (1947).

[15] K. Yoshizawa, T. Kato, and T. Yamabe, J. Chem. Phys. **105**, 2099 (1996).

[16] X. F. Wang, Phys. Rev. B **72**, 085317 (2005).

[17] Kenneth W.-K. Shung, Phys. Rev. B **34**, 979 (1986); P. B. Visscher and L. M. Falicov, *ibid.* **3**, 2541 (1971).